Biomedical Optics EXPRESS

In vivo imaging of retinal pigment epithelium cells in age related macular degeneration

Ethan A. Rossi,[1,*] Piero Rangel-Fonseca,[2] Keith Parkins,[1] William Fischer,[3] Lisa R. Latchney,[3] Margaret A. Folwell,[1] David R. Williams,[1,4] Alfredo Dubra[5,6] and Mina M. Chung[1,3]

[1]*Center for Visual Science, University of Rochester, 601 Elmwood Avenue, Rochester, NY 14642, USA*
[2]*Centro de Investigaciones en Óptica, Loma del Bosque 115, Lomas del Campestre, León, Gto. 37150, Mexico*
[3]*Flaum Eye Institute, University of Rochester, 601 Elmwood Avenue, Rochester, NY 14642, USA*
[4]*The Institute of Optics, University of Rochester, 601 Elmwood Avenue, Rochester, NY 14642, USA*
[5]*Department of Ophthalmology, Medical College of Wisconsin, 925 N 87th Street, Milwaukee, WI 53226, USA*
[6]*Department of Biophysics, Medical College of Wisconsin, 925 N 87th Street, Milwaukee, WI 53226, USA*
**erossi@cvs.rochester.edu*

Abstract: Morgan and colleagues demonstrated that the RPE cell mosaic can be resolved in the living human eye non-invasively by imaging the short-wavelength autofluorescence using an adaptive optics (AO) ophthalmoscope. This method, based on the assumption that all subjects have the same longitudinal chromatic aberration (LCA) correction, has proved difficult to use in diseased eyes, and in particular those affected by age-related macular degeneration (AMD). In this work, we improve Morgan's method by accounting for chromatic aberration variations by optimizing the confocal aperture axial and transverse placement through an automated iterative maximization of image intensity. The increase in image intensity after algorithmic aperture placement varied depending upon patient and aperture position prior to optimization but increases as large as a factor of 10 were observed. When using a confocal aperture of 3.4 Airy disks in diameter, images were obtained using retinal radiant exposures of less than 2.44 J/cm^2, which is ~22 times below the current ANSI maximum permissible exposure. RPE cell morphologies that were strikingly similar to those seen in postmortem histological studies were observed in AMD eyes, even in areas where the pattern of fluorescence appeared normal in commercial fundus autofluorescence (FAF) images. This new method can be used to study RPE morphology in AMD and other diseases, providing a powerful tool for understanding disease pathogenesis and progression, and offering a new means to assess the efficacy of treatments designed to restore RPE health.

OCIS codes: (110.1080) Active or adaptive optics; (330.5310) Vision - photoreceptors; (170.1610) Clinical applications; (170.3880) Medical and biological imaging; (170.4470) Ophthalmology.

References and links

1. C. J. Blair, "Geographic atrophy of the retinal pigment epithelium. A manifestation of senile macular degeneration," Arch. Ophthalmol. **93**(1), 19–25 (1975).
2. J. D. Gass, "Drusen and disciform macular detachment and degeneration," Trans. Am. Ophthalmol. Soc. **70**, 409–436 (1972).
3. W. R. Green, P. J. McDonnell, and J. H. Yeo, "Pathologic features of senile macular degeneration," Ophthalmology **92**(5), 615–627 (1985).
4. H. Kaneko, S. Dridi, V. Tarallo, B. D. Gelfand, B. J. Fowler, W. G. Cho, M. E. Kleinman, S. L. Ponicsan, W. W. Hauswirth, V. A. Chiodo, K. Karikó, J. W. Yoo, D. K. Lee, M. Hadziahmetovic, Y. Song, S. Misra, G. Chaudhuri, F. W. Buaas, R. E. Braun, D. R. Hinton, Q. Zhang, H. E. Grossniklaus, J. M. Provis, M. C. Madigan, A. H. Milam, N. L. Justice, R. J. C. Albuquerque, A. D. Blandford, S. Bogdanovich, Y. Hirano, J. Witta, E. Fuchs, D. R. Littman, B. K. Ambati, C. M. Rudin, M. M. W. Chong, P. Provost, J. F. Kugel, J. A. Goodrich, J. L. Dunaief, J. Z. Baffi, and J. Ambati, "DICER1 deficit induces Alu RNA toxicity in age-related macular degeneration," Nature **471**(7338), 325–330 (2011).

#197058 - $15.00 USD Received 3 Sep 2013; revised 9 Oct 2013; accepted 12 Oct 2013; published 18 Oct 2013

5. M. Rudolf, S. D. Vogt, C. A. Curcio, C. Huisingh, G. McGwin, Jr., A. Wagner, S. Grisanti, and R. W. Read, "Histologic basis of variations in retinal pigment epithelium autofluorescence in eyes with geographic atrophy," Ophthalmology **120**(4), 821–828 (2013).
6. R. Adler, C. Curcio, D. Hicks, D. Price, and F. Wong, "Cell death in age-related macular degeneration," Mol. Vis. **5**, 31 (1999).
7. F. C. Delori, M. R. Fleckner, D. G. Goger, J. J. Weiter, and C. K. Dorey, "Autofluorescence distribution associated with drusen in age-related macular degeneration," Invest. Ophthalmol. Vis. Sci. **41**(2), 496–504 (2000).
8. A. von Rückmann, F. W. Fitzke, and A. C. Bird, "Distribution of fundus autofluorescence with a scanning laser ophthalmoscope," Br. J. Ophthalmol. **79**(5), 407–412 (1995).
9. A. von Rückmann, F. W. Fitzke, and A. C. Bird, "In vivo fundus autofluorescence in macular dystrophies," Arch. Ophthalmol. **115**(5), 609–615 (1997).
10. A. von Rückmann, F. W. Fitzke, and A. C. Bird, "Fundus autofluorescence in age-related macular disease imaged with a laser scanning ophthalmoscope," Invest. Ophthalmol. Vis. Sci. **38**(2), 478–486 (1997).
11. A. von Rückmann, F. W. Fitzke, J. Fan, A. Halfyard, and A. C. Bird, "Abnormalities of fundus autofluorescence in central serous retinopathy," Am. J. Ophthalmol. **133**(6), 780–786 (2002).
12. F. G. Holz, A. Bindewald-Wittich, M. Fleckenstein, J. Dreyhaupt, H. P. N. Scholl, and S. Schmitz-Valckenberg; FAM-Study Group, "Progression of geographic atrophy and impact of fundus autofluorescence patterns in age-related macular degeneration," Am. J. Ophthalmol. **143**(3), 463–472, 472.e2 (2007).
13. J. C. Hwang, J. W. K. Chan, S. Chang, and R. T. Smith, "Predictive value of fundus autofluorescence for development of geographic atrophy in age-related macular degeneration," Invest. Ophthalmol. Vis. Sci. **47**(6), 2655–2661 (2006).
14. R. G. Sayegh, C. Simader, U. Scheschy, A. Montuoro, C. Kiss, S. Sacu, D. P. Kreil, C. Prünte, and U. Schmidt-Erfurth, "A systematic comparison of spectral-domain optical coherence tomography and fundus autofluorescence in patients with geographic atrophy," Ophthalmology **118**(9), 1844–1851 (2011).
15. F. Delori, J. P. Greenberg, R. L. Woods, J. Fischer, T. Duncker, J. Sparrow, and R. T. Smith, "Quantitative measurements of autofluorescence with the scanning laser ophthalmoscope," Invest. Ophthalmol. Vis. Sci. **52**(13), 9379–9390 (2011).
16. D. C. Gray, W. Merigan, J. I. Wolfing, B. P. Gee, J. Porter, A. Dubra, T. H. Twietmeyer, K. Ahamd, R. Tumbar, F. Reinholz, and D. R. Williams, "In vivo fluorescence imaging of primate retinal ganglion cells and retinal pigment epithelial cells," Opt. Express **14**(16), 7144–7158 (2006).
17. J. I. W. Morgan, A. Dubra, R. Wolfe, W. H. Merigan, and D. R. Williams, "In vivo autofluorescence imaging of the human and macaque retinal pigment epithelial cell mosaic," Invest. Ophthalmol. Vis. Sci. **50**(3), 1350–1359 (2008).
18. E. A. Rossi, M. M. Chung, A. Dubra, H. Song, and D. R. Williams, "Tracking disease progression in geographic atrophy with adaptive optics imaging," presented at Engineering the Eye III, Benasque, Spain, 10 June 2011.
19. E. A. Rossi, D. R. Williams, A. Dubra, H. Song, M. A. Folwell, L. R. Latchney, and M. M. Chung, "Photoreceptor and RPE Disruptions Observed Outside Clinically Visible Geographic Atrophy Lesions in the Living Eye with Fluorescence Adaptive Optics Scanning Laser Ophthalmoscopy (FAOSLO)," Invest. Ophthalmol. Vis. Sci. **53**, E–Abstract 5599 (2012).
20. A. Dubra and Y. Sulai, "Reflective afocal broadband adaptive optics scanning ophthalmoscope," Biomed. Opt. Express **2**(6), 1757–1768 (2011).
21. D. H. Brainard, "The psychophysics toolbox," Spat. Vis. **10**(4), 433–436 (1997).
22. M. Kleiner, D. Brainard, and D. G. Pelli, "What's new in Psychtoolbox-3?" Perception **36**, (2007).
23. D. G. Pelli, "The VideoToolbox software for visual psychophysics: Transforming numbers into movies," Spat. Vis. **10**(4), 437–442 (1997).
24. American National Standards Institute, *American National Standard for Safe Use of Lasers* (ANSI Z136.1–2007).
25. E. A. Rossi and J. J. Hunter, *Rochester Exposure Limit Calculator [Computer software]* (University of Rochester, 2013). *http://aria.cvs.rochester.edu/software/RELcalculator.html*
26. J. I. W. Morgan, J. J. Hunter, B. Masella, R. Wolfe, D. C. Gray, W. H. Merigan, F. C. Delori, and D. R. Williams, "Light-induced retinal changes observed with high-resolution autofluorescence imaging of the retinal pigment epithelium," Invest. Ophthalmol. Vis. Sci. **49**(8), 3715–3729 (2008).
27. J. I. W. Morgan, J. J. Hunter, W. H. Merigan, and D. R. Williams, "The reduction of retinal autofluorescence caused by light exposure," Invest. Ophthalmol. Vis. Sci. **50**(12), 6015–6022 (2009).
28. F. C. Delori, R. H. Webb, and D. H. Sliney, "Maximum permissible exposures for ocular safety (ANSI 2000), with emphasis on ophthalmic devices," J. Opt. Soc. Am. A **24**(5), 1250–1265 (2007).
29. M. F. Marmor and T. J. Wolfensberger, eds., *The Retinal Pigment Epithelium: Function and Disease* (Oxford University Press, 1998).
30. E. Fernández, A. Unterhuber, P. Prieto, B. Hermann, W. Drexler, and P. Artal, "Ocular aberrations as a function of wavelength in the near infrared measured with a femtosecond laser," Opt. Express **13**(2), 400–409 (2005).
31. L. N. Thibos, M. Ye, X. Zhang, and A. Bradley, "The chromatic eye: a new reduced-eye model of ocular chromatic aberration in humans," Appl. Opt. **31**(19), 3594–3600 (1992).
32. F. C. Delori, C. K. Dorey, G. Staurenghi, O. Arend, D. G. Goger, and J. J. Weiter, "In vivo fluorescence of the ocular fundus exhibits retinal pigment epithelium lipofuscin characteristics," Invest. Ophthalmol. Vis. Sci. **36**(3), 718–729 (1995).
33. J. I. W. Morgan, "In vivo imaging of the retinal pigment epithelial cells," (University of Rochester, 2008).

#197058 - $15.00 USD Received 3 Sep 2013; revised 9 Oct 2013; accepted 12 Oct 2013; published 18 Oct 2013

34. K. Grieve, P. Tiruveedhula, Y. Zhang, and A. Roorda, "Multi-wavelength imaging with the adaptive optics scanning laser ophthalmoscope," Opt. Express **14**(25), 12230–12242 (2006).
35. J. A. Nelder and R. Mead, "A Simplex Method for Function Minimization," Comput. J. **7**(4), 308–313 (1965).
36. J. Borggaard, *NELDER_MEAD[Computer software]* (2009). *http://people.sc.fsu.edu/~jburkardt/m_src/nelder_mead/nelder_mead.html*
37. A. Dubra and Z. Harvey, "Registration of 2D Images from Fast Scanning Ophthalmic Instruments," in *Biomedical Image Registration*, B. Fischer, B. M. Dawant, and C. Lorenz, eds., Lecture Notes in Computer Science No. 6204 (Springer Berlin Heidelberg, 2010), pp. 60–71.
38. P. Rangel-Fonseca, A. Gomez-Vieyra, D. Malacara-Hernández, M. C. Wilson-Herran, M. M. Chung, D. R. Williams, and E. A. Rossi, University of Rochester, 601 Elmwood Avenue, Rochester, NY 14642 are preparing a manuscript to be called "Automated segmentation of retinal pigment epithelium cells in fluorescence adaptive optics images."
39. D. H. Sliney, J. J. Hunter, F. C. Delori, D. R. Williams, and J. Mellerio, "Competing Photochemical Retinal Damage Mechanisms From Visible Light: Implications for Human Retinal Exposure Limits," Invest. Ophthalmol. Vis. Sci. **51**, E-Abstract 3456 (2010).

1. Introduction

Drusen and atrophy of the retinal pigment epithelium (RPE) are hallmarks of age related macular degeneration (AMD) [1–3]. Histological studies of postmortem eyes have shown that substantial changes occur in RPE cell mosaic morphology in AMD [4,5]. These changes may precede and/or accompany RPE cell death and the degeneration of overlying photoreceptors [4,6]. Clinical imaging methods, such as confocal scanning laser ophthalmoscopy (cSLO), are used to examine the FAF pattern as a means of assessing the health of the RPE in AMD and other retinal diseases [7–11]. However, currently available commercial fundus autofluorescence (FAF) imaging systems lack the resolution to identify individual cells, preventing morphometric analysis of the RPE cell mosaic.

Recent advances in imaging the intrinsic autofluorescence (AF) of lipofuscin have shown promise in its ability to assess the health and integrity of the RPE. FAF images obtained using commercial instruments have demonstrated utility for observing the overall patterns of RPE fluorescence seen in disease, and can be useful for assessing the extent of RPE loss in geographic atrophy (GA) and its progression rate [12]. Classification schemes have been proposed to identify subtypes associated with more rapid progression, but a percentage of patients could not be classified according to the system [12], and these findings were not replicated in another study [13]. The total absence of an FAF signal is often interpreted as complete RPE atrophy; however, spectral domain optical coherence tomography (SD-OCT) has been shown to be more precise for measuring lesion size in GA [14]. Variability in fluorescence seen at the borders of GA lesions and by screening of fluorescence due to macular pigment (particularly for 488 nm excitation) may introduce errors in measurement of GA lesion size using FAF. Additionally, since the fluorescence signal obtained is not a radiometric measurement (ie. the images display relative not absolute AF), the interpretation of hyper AF and hypo AF patterns seen in diseased eyes is difficult. A method to quantify AF by standardizing measurements to an internal control has been developed [15]; however, it is not an absolute measure of lipofuscin because of light losses in the ocular tissues.

Patterns of hyper AF and hypo AF presumably relate to changes in the health and integrity of the RPE cell mosaic, but cellular resolution is needed to understand how RPE cell mosaic morphology relates to the patterns seen in FAF images. Histological studies have shown that RPE mosaic morphology is drastically altered in AMD [4,5], but these studies of post mortem eyes are limited in that they only reveal a single time point and cannot compare changes in RPE morphology to other measures, such as cSLO FAF imaging, SD-OCT, or AO reflectance imaging of the photoreceptor cell mosaic. *In vivo* cellular resolution imaging has the potential to identify early disease changes in the RPE cell mosaic, before the heterogeneous patterns of hyper AF and hypo AF seen in conventional FAF imaging arise. Furthermore, cellular imaging could enable earlier detection of retinal disease, improved understanding of disease etiology, more rapid monitoring of disease progression, and more sensitive metrics for evaluating treatment effects.

By combining fluorescence imaging methods with adaptive optics scanning light ophthalmoscopy (FAOSLO), Gray, Morgan and colleagues demonstrated that it was possible

#197058 - $15.00 USD Received 3 Sep 2013; revised 9 Oct 2013; accepted 12 Oct 2013; published 18 Oct 2013

to image individual RPE cells *in vivo* in monkeys [16]. Morgan and colleagues later demonstrated that these methods could be used to achieve single cell resolution of the RPE in the living human eye [17]. Since the RPE is important for maintaining the healthy function of the photoreceptor layer and is implicated in many retinal diseases, such as AMD [7–11], the demonstration that these cells were now accessible to optical imaging in the living human eye was a potentially valuable advance. However, our early attempts to image the RPE in patients with AMD using these methods proved difficult; we were able to obtain images with greater structural detail than commercial systems, but individual cells could not be resolved [18,19].

The reason for this is that the aging eye poses a challenge for imaging, even for adaptive optics ophthalmic imaging instruments. Optical challenges that affect image contrast and resolution include increased scatter, lens opacities and dry eye. Patients with AMD whose central vision is compromised usually have poor fixation, which can increase distortions in scanning system images and make image registration difficult. Moreover, older adults can often have other health problems or mobility issues requiring imaging sessions to be short. All of these factors conspire to make imaging the aging eye more difficult than younger eyes. Despite having success imaging RPE cells in some healthy young eyes using the fixed dual focus method proposed by Morgan and colleagues, our ability to resolve the RPE mosaic was highly inconsistent. This was due in part to poor compensation of the longitudinal chromatic aberration (LCA) of the eye. This procedure proved difficult to replicate reliably using manual positioning of the optical elements, such as lenses, light sources and confocal aperture. This is supported by early experiments that suggested that a fixed defocus offset to compensate for chromatic aberration did not appear to work consistently for all observers. This inconsistency was due to a combination of optical alignment and true differences in LCA between participants. We therefore sought to address both problems by controlling the position of the fluorescence light source and detector in a reliable and reproducible manner in an automated way.

2. Methods

2.1 Participants

Participants with AMD were recruited from the faculty practice of the Flaum Eye Institute at the University of Rochester Medical Center. Normal controls were recruited from the University of Rochester community. All participants were phakic. All participants gave written informed consent after the nature of the research and possible risks were explained both verbally and in writing. All experiments were approved by the Research Subjects Review Board of the University of Rochester and adhered to the tenets of the Declaration of Helsinki.

2.2 Clinical imaging

Color fundus photography was performed on all participants. Patients underwent further clinical imaging using commercial cSLO (Spectralis HRA + OCT, Heidelberg Engineering, Germany). cSLO images (field of view: 30° × 30°) were obtained in both infrared reflectance and FAF imaging modes. FAF images were acquired on separate days from AO fluorescence imaging to limit cumulative daily visible light exposures. FAF images were used to assess the overall pattern of RPE fluorescence and in some cases to guide imaging sessions to areas of interest (see section on wide field fundus image guided targeting below).

2.3 FAOSLO imaging

We used a broadband FAOSLO nearly identical in optical design to one described in detail elsewhere [20]. Only relevant system parameters and the modifications to the light delivery and detection portions of the system that we made to implement our new methods will be discussed here. The size of the FAOSLO imaging field subtended ~1.5° × 1.5° on the retina and image sequences were acquired at ~20 Hz. For AF imaging, three wavelengths of light were simultaneously delivered for wavefront sensing, infrared (IR) imaging, and fluorescence

#197058 - $15.00 USD Received 3 Sep 2013; revised 9 Oct 2013; accepted 12 Oct 2013; published 18 Oct 2013

excitation. Wavefront sensing used an 847 nm laser diode (QFLD-850-10SB-PM, QPhotonics, LLC, Ann Arbor, MI, USA), IR reflectance imaging used a 796 nm (14nm FWHM) superluminescent diode (Inphenix, Inc., Livermore, CA), and fluorescence excitation was stimulated using a 532 nm laser diode module (FiberTec II, Blue Sky Research, Milpitas, CA).

To ensure stable power output of the 532 nm excitation source, a fiber-coupled feedback collimator (FiberTec II Fiber Feedback Collimator (FFC), Blue Sky Research, Milpitas, CA) was used; the FFC provided ~0.5% power stability (manufacturer specification). A computer controlled electronic shutter (04IES211, CVI Melles-Griot, Rochester, NY, USA) placed in front of the FFC controlled visible light exposure duration. The collimated beam that emerged from the FFC was too small for our purposes (1.37 mm), so we used a long working distance 20X microscope objective (ULWD CDPlan20, Olympus Corporation, Tokyo, Japan) to expand the beam. The microscope objective focused the light onto a 5 μm aperture; this spatially filtered the light and effectively produced a point source for illumination. Light emerging from the spatial filter was focused using an 80 mm focal length positive achromatic lens (Linos G0631430000, Qioptiq, Inc., Fairport, NY, USA). The achromatic lens was mounted onto a motorized translation stage (MTS-50, Thorlabs, Newton, NJ, USA) so that the vergence of the light at the entrance pupil could be precisely controlled; details on dual focus settings and automation for optimizing LCA compensation are provided below. When placed at its collimated position, the diameter of the beam that emerged filled the entire lens (22 mm). The beam profile was approximately Gaussian; an aperture at the entrance pupil of the system allowed only the central 7.25 mm portion of the beam into the instrument.

2.4 Wide field fundus image guided targeting

We used a computer controlled fixation target to position the FAOSLO imaging field to specific retinal locations. The target was typically a white circle (the size was varied depending upon the visual acuity of the patient) that was projected onto the ceiling using a DLP projector and viewed off an anti-reflection coated laser window (W1-IF-3050-C-633-1064-45UNP, CVI Melles-Griot, Rochester, NY, USA) placed in front of the eye. The fixation target was produced and controlled with a custom MATLAB (MathWorks, Natick, MA, USA) graphical user interface (GUI). The target stimulus was generated and controlled using elements of the Psychophysics toolbox extensions [21–23].

The GUI allowed the experimenter to load in a wide field fundus image obtained with a clinical instrument (such as a fundus photograph or cSLO image), calibrate the magnification and offset for the location of the FAOSLO imaging field, and then use the software to target specific locations using the fundus image as a map. Vascular features in the wide field fundus image were compared to those in the live AO IR reflectance image to ensure that the patient was fixating on the target and that the mapping between images was accurate. A small square overlaid on the fundus image displayed in the GUI indicated the location being targeted; as the fixation target and thus the observer's eye were moved, this mark moved across the wide field fundus image. The GUI communicated through a network connection to the image recording software that ran on a separate PC and automatically marked recorded locations on the fundus image whenever an image sequence was acquired. This provided the experimenter with feedback as to which locations had been imaged, preventing repeat imaging of the same location (and thus overexposure to visible light). The GUI displayed the retinal coordinates of each location and saved the coordinates to a text file as each image sequence was acquired. At the end of each imaging session, the fundus image, with each recording location marked as an overlaid square, was saved; these images were later used as a guide (along with the text file of recording coordinates) for montaging of images and to map FAOSLO images to their corresponding locations on wide field fundus images. For many participants, the projected stimulus was too dim for them to see when the fluorescence excitation light came on; in those cases a laser pointer was pointed at the projected target on the screen to provide a brighter target for fixation.

#197058 - $15.00 USD Received 3 Sep 2013; revised 9 Oct 2013; accepted 12 Oct 2013; published 18 Oct 2013

2.5 Light safety

Light source power levels and exposure durations were used that are well below the maximum permissible exposure (MPE) specified by the American National Standards Institute (ANSI) standard for the Safe Use of Lasers, ANSI Z136.1-2007 [24]. We used ~14 μW of 847 nm light for wavefront sensing, ~140 μW of 796 nm light for infrared imaging, and 35-40 μW of 532 nm light for fluorescence excitation. Powers were kept constant and exposure durations were limited to ensure safety. We stayed below our own Rochester Exposure Limit (REL) [25], which is partially based on the ANSI but which we have devised to be much more conservative, especially in the visible wavelength range. We developed the photochemical REL based on previous data from Morgan et al. that showed changes in monkey RPE AF after exposure to visible light levels below the ANSI limit [26,27]. The REL software calculations ensured that the combined exposure to all three wavelengths simultaneously was safe; the calculations it performs are based on published methods for calculating contributions for multi-wavelength ocular exposures [28]. We used a custom software program to calculate the REL before each imaging session [25]. For 40 μW, the REL specified that the maximum duration of 532 nm light exposure at any given retinal location was ~120 seconds (~22 times lower than the ANSI MPE). This power and exposure duration resulted in retinal radiant exposures less than 2.44 J/cm^2, the ANSI "blue light hazard" for the range 400–450 nm [24,28]. The visible light appeared bright but was well tolerated by the patients and controls. We exposed a single location to all three light sources simultaneously for ~90 seconds. Since we used ~75% our full exposure duration at each location imaged, we used our fixation target software and vascular landmarks to ensure that each imaging location was spaced sufficiently from adjacent imaging locations so that fixational drifts or microsaccades did not cause exposure locations to overlap. The IR light levels used could be viewed continuously for the maximum duration specified by ANSI Z136.1-2007 (30,000 seconds). We imaged a single location for a maximum of ~5 minutes using just the infrared light sources, so the total infrared exposure duration was ~7 minutes at each location (~10 and ~124 times lower than the ANSI MPE for the IR and wavefront sensing light sources, respectively).

2.6 Dual-focus, fixed offset procedure

To maximize data collection efficiency, our goal was to simultaneously acquire images of the photoreceptor layer in IR and of the RPE in fluorescence. To accomplish this, the IR light must be focused on the photoreceptors, while the fluorescence excitation light is focused on the RPE. The focus of the photoreceptor and RPE layers should be very close to one another axially, as the photoreceptor outer segments are in contact with the apical processes of the RPE cells [29]. If each wavelength were to enter the eye collimated, LCA would cause the longer wavelength of light to focus deeper than the shorter wavelength. Therefore, an appropriate amount of focus offset between the two sources must be achieved to cause them to focus at the same axial position. Additionally, since the wavelength of light emitted from the lipofuscin in the RPE is different than the wavelength used for excitation, the confocal aperture must be placed appropriately for the emission bandwidth of the fluorescence emission filter. All of this positioning must be done appropriately to compensate for the chromatic aberration of the eye and obtain in focus images of the RPE. We started by setting a fixed focus offset that minimized LCA based upon published measures [30,31].

The first step towards setting this fixed focus offset was to get each source in focus in reflectance imaging mode, on a model eye with no chromatic aberration, which consisted of a lens and a piece of paper upon which many small (9.9 μm diameter) fluorescent beads (FS06F, Bangs Laboratories, Inc., Fishers, IN, USA) had been deposited. We began by making the 532 nm light collimated using a shear plate. We then manually adjusted the focus of the light using the deformable mirror to bring the image of the paper into sharp focus. The position of the PMT and confocal aperture was then adjusted to maximize throughput. We used a large confocal aperture (~3.4 times the Airy disc diameter at 650 nm), and iterated

#197058 - $15.00 USD Received 3 Sep 2013; revised 9 Oct 2013; accepted 12 Oct 2013; published 18 Oct 2013

between adjusting the focus using the DM and adjusting the confocal aperture position until the best subjective image quality was achieved. The next step was to place the confocal aperture to maximize the detection of the light that would be emitted by the RPE. The emission filter was placed in front of the PMT detector so that we could visualize the fluorescent beads. To maximize light collection across the bandwidth of lipofuscin emission [32], we used a filter with a broad band pass (150 nm) centered at 650 nm (BrightLine FF01-650/150-25, Semrock, Inc., Rochester, NY, USA). After the filter was placed, pinhole positioning was done using the automated method described below. Once the fluorescence channel was set, the IR channel was adjusted to obtain an in focus image of the paper (in reflectance). This was done by translating the tip of the fiber of the 796 nm SLD (which was mounted on a manual micrometer) and adjusting both the axial position of the lens in front of the confocal aperture and the lateral position of the confocal aperture iteratively until the best subjective image of the paper was obtained. This procedure would have been sufficient for configuring the system for AF imaging if the eye did not have any chromatic aberration.

However, if adjustments were not made to compensate for the chromatic aberration of the eye, when the 796 nm light was focused on the photoreceptors, the 532 nm excitation light would be focused on the inner retina. As a first step towards LCA compensation, we used published measurements of the LCA of the human eye [30,31] to determine the dioptric difference in focus (or vergence) needed to compensate for this LCA. After Morgan [33], we used the dioptric difference between the 532 nm excitation wavelength and 796 nm reflectance wavelength to calculate the vergence offset needed for the ingoing light and the difference between the reflectance wavelength and the center of the emission band pass filter (650 nm) to determine the outgoing LCA compensation needed. The ingoing 532 nm light was defocused 0.99 D by translating the lens in front of the spatial filter 9 mm. The LCA compensation for the outgoing light (0.36 D) was made by translating the confocal aperture 3.74 mm. We calculated the distances required to move these elements to achieve the desired focus offsets using a simple geometrical optics model of the system, which took into account the distances between the collimating lens and entrance pupil (~330 mm), system magnification (1.067), and focal lengths of lenses at the source (80 mm) and detector (100 mm). We ensured that the movements we made were precise and repeatable by controlling each with optically encoded piezoelectric actuators (MTS-50 for the collimating lens and Z812B for the detector; Thorlabs, Inc., Newton, NJ, USA).

2.7 Automatic focus refinement

The focus offset procedure outlined above brought us close to achieving the desired LCA compensation; however, in practice we found that the best focus was usually slightly different from these fixed offsets for each individual. The only solution to this problem seemed to be to acquire several different image sequences at multiple foci, with the hope that one of them would be in focus. Since we were limited to only 120 seconds at each location, and it took ~20-30 seconds to obtain enough frames to generate a high signal to noise ratio image of the RPE, this method only allowed perhaps 3-4 different foci to be obtained. As the appropriate focus was unknown, this method was inefficient and impractical and often the best focus was never obtained in the few attempts we had at each location. It was clear from these early experiments that a small amount of chromatic aberration remained that needed to be compensated for. We therefore developed an automated procedure to determine the focus that gave the highest intensity fluorescence signal. As previously mentioned, an algorithmic method for true auto focusing (ie. one that used an objective image quality metric) could not be used, as each frame in the image contained too little signal to provide a meaningful measurement. However, small focus differences do result in quantifiable changes in fluorescence intensity. These small changes in intensity resulting from small differences in focus are very difficult to appreciate with the naked eye, but can be quantified reliably using a computer algorithm. We used a very simple approach to determine the focus with peak fluorescence intensity. The deformable mirror, under computer control, was used to step through several different foci around the defocus setting that gave the best cone image in the

#197058 - $15.00 USD Received 3 Sep 2013; revised 9 Oct 2013; accepted 12 Oct 2013; published 18 Oct 2013

reflectance imaging channel. At each foci, a small number of frames were acquired (~5-10); the mean pixel value was computed for each frame and then the average was computed for all frames acquired at that focus. Typically, a fixed number of frames were averaged at each interval, although this varied as we refined the process to use fewer frames. In our early experiments, we kept the shutter open during this entire process (~30 seconds); however, we found that it took a second or two of software and hardware latency for the focus shape to be placed on the DM and the AO to converge. In our later implementations, we closed the shutter between each focus interval. This minimized light exposure during the automated focus procedure to ~10 seconds, allowing more of our limited exposure duration at each location to be used for imaging.

2.8 Automatic confocal aperture alignment

The automatic focus refinement procedure described above allowed us to find the focus needed to obtain the highest fluorescence signal. However, the chromatic aberration of the fluorescent light still required refinement. Because we used a relatively large pinhole, and a broad band pass filter, we were much less sensitive to LCA on the detection side. TCA, however, remained a problem. The TCA of the eye and system between the excitation and emission wavelengths causes the focused spot at the confocal aperture to be displaced laterally relative to where it was on the model eye. TCA causes a slight lateral misalignment of the confocal aperture when the human eye is imaged. TCA can arise due to either the system or the eye, or both. Additionally, as the human eye moves and the pupil position changes, the TCA changes as well. Grieve and colleagues [34] measured the TCA between 532 nm and 658 nm using an AOSLO and found a range of 48-142 arc seconds; they also measured TCA variation across the central 2.5 mm of the pupil and found that it varied by 100 arc seconds. Since the confocal aperture is large, we still get some signal through in these misaligned positions, but we found that we could greatly improve signal throughput if we adjusted the confocal aperture slightly to optimize signal intensity. This was impossible to do manually, as we needed to optimize the pinhole position based upon very small intensity fluctuations and by making extremely small movements of the aperture, all in a relatively short time with the eye constantly in motion (which also caused small fluctuations in single frame intensities). However, we found that this problem was solvable with an automated algorithmic control method.

The problem of optimizing light coupling into an optical system, such as the alignment of optical fibers, is one that has been studied extensively and has been solved successfully using several different algorithmic methods. This problem of maximizing light coupling in a multidimensional space is analogous to the problem we faced. One algorithm that has been successfully employed for this purpose is the Nelder-Mead optimization algorithm [35]. The detector was motorized and the Nelder-Mead optimization algorithm was implemented using functions from the MATLAB program NELDER_MEAD [36]. The PMT was mounted on a three-axis translation stage (RB13, Thorlabs Inc., Newton, NJ) and each axis was equipped with an optically encoded piezoelectric actuator (Z812B, Thorlabs Inc., Newton, NJ). These actuators allowed for extremely small movements (0.05 μm) to be made under computer control by interfacing the motors using the APT control software extensions (Thorlabs, Inc., Newton, NJ), which we implemented in a MATLAB control GUI. The distance between the aperture and detector was fixed by attaching the confocal aperture to the PMT using a lens tube, so they moved together in three dimensions. The implementation of the Nelder-Mead algorithm was validated using a model eye by measuring the intensity of the signal at the detector for a matrix of points around the point spread function. We did this for both the model eye in reflectance using a ~1.2 Airy disc pinhole (20 um at 532 nm) and in fluorescence using the ~3.4 Airy disc pinhole (75 um at 650 nm). We used these setups to test different algorithm constants, such as the tolerance, which determined simplex convergence, and to determine the search space required to optimize Nelder-Mead performance. Algorithm performance was characterized for randomly determined starting positions whose locations were generated using the rand command in MATLAB.

#197058 - $15.00 USD Received 3 Sep 2013; revised 9 Oct 2013; accepted 12 Oct 2013; published 18 Oct 2013

2.9 Dual-registration

We used the dual registration method described previously [17] to register the AF images using the motion from the IR reflectance channel. Briefly, this method uses cross-correlation to register the reflectance IR images and applies the calculated motion shifts to the AF images. Registered images were then averaged to obtain a high signal to noise ratio image; we typically averaged around 1160 autofluorescence images to obtain an image of the RPE cell mosaic. For efficiency, we used the data from both the forward and backward scans; the sinusoidal distortion from the resonant scan pattern was removed and forward and backward scan images were interleaved prior to registration. We used in-house software to perform strip-based registration [37].

2.10 RPE cell segmentation and analysis

An early version of a cell segmentation algorithm [38], developed in-house and implemented in MATLAB (MathWorks, Natick, MA, USA), was used to extract the boundaries of individual RPE cells. Briefly, the algorithm used several image processing steps, including smoothing, edge detection, edge correction and binarization to produce a binary image of the borders of RPE cells. Segmentation was verified by overlaying the algorithmically segmented binary image on the original image in Adobe Photoshop CS4 (Adobe Systems Inc., San Jose, CA, USA). Errors in segmentation were then corrected manually using the pencil tool in Photoshop, prior to morphometric analysis. Binary images were then analyzed using MATLAB and statistical analyses were performed in either MATLAB or Excel (Microsoft Corporation, Redmond, WA, USA). Cell areas were calculated in MATLAB by summing the number of pixels that fell within each segmented region and multiplying by the area of a single pixel. Pixel dimensions were calculated for each participant by using a Gullstrand #2 simplified relaxed schematic eye model, scaled by the axial length of the eye measured with an IOL master (CarlZeiss Meditec, Inc., Germany).

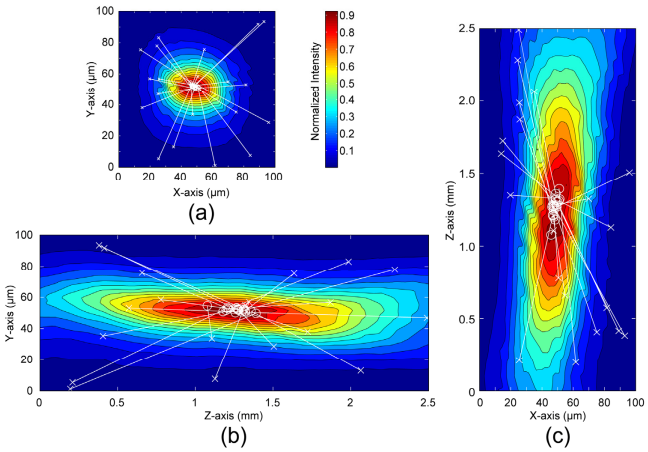

Fig. 1. Nelder-Mead algorithm validated on a model eye. The start (white x's) and end positions (white o's) for 20 random starting points are overlaid on the intensity profile of the focused spot; solid lines link start and end positions and do not represent the algorithm path. Panels (a)-(c) show different views of the same data sliced at the maximum intensity position, showing coronal (a), side (b) and overhead (c) views. Note the difference in scale between the (x,y) and (z) dimensions. Color bar shows relation between color and normalized intensity.

3. Results

The Nelder-Mead simplex algorithm performed well when tested on a model eye, both in reflectance (Fig. 1) and in fluorescence (not shown). Results in humans showed that the algorithm was in most cases able to increase the signal substantially, but that the change in intensity varied depending on the starting position. In some cases the confocal aperture was

#197058 - $15.00 USD Received 3 Sep 2013; revised 9 Oct 2013; accepted 12 Oct 2013; published 18 Oct 2013

close to the optimal location, so the increase in intensity was negligible, in other cases it was far from its optimal location and we saw increases of up to a factor of 10 in intensity. This variability in the starting position makes it difficult to quantify the performance in an objective way. The greatest intensity increase was usually observed during the first run of the Nelder-Mead algorithm, as the starting position for this run was from the position that the confocal aperture was set to on the model eye. The Nelder-Mead algorithm sometimes did not converge during the 30 second exposures that we typically used. This was often due to the Nelder-Mead tolerance variable being too low for the algorithm to reach convergence. In these cases we either chose the position setting with the highest intensity during that run or reset it to the value from the previous run.

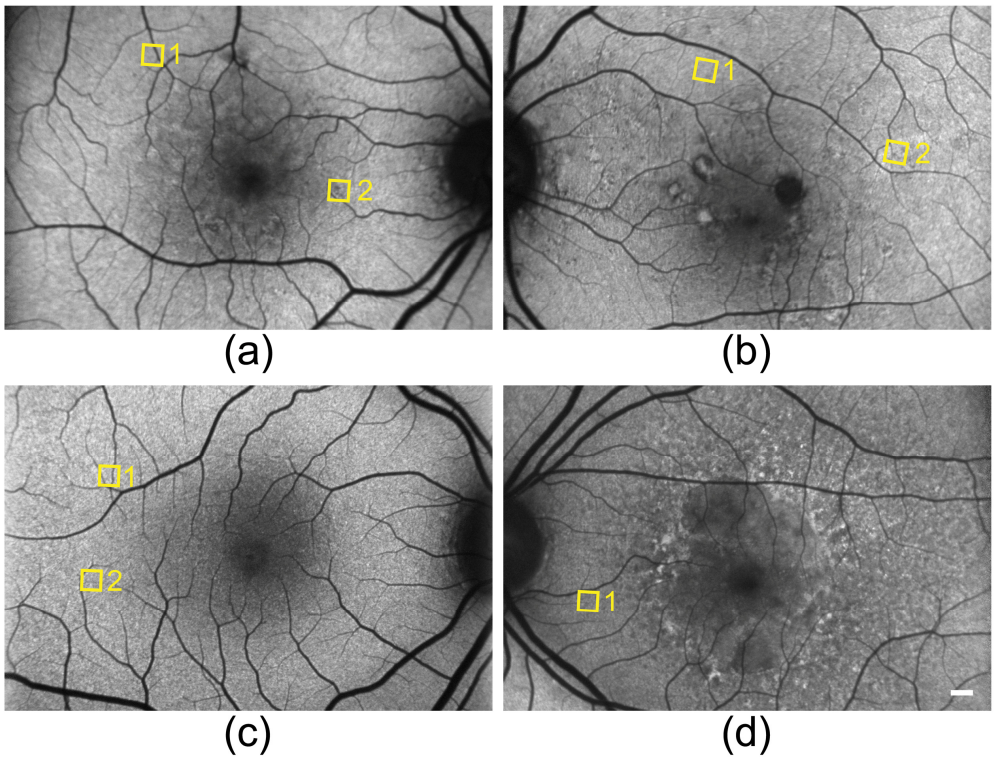

Fig. 2. Wide field FAF cSLO images and FAOSLO image locations. Images for subjects AMD1, AMD2, normal young healthy control & AMD3 are shown in panels (a), (b), (c), & (d), respectively. FAOSLO image locations shown in subsequent figures are outlined in yellow. Scale bar is 400 µm.

Wide field FAF images of each subject are shown in Fig. 2, with FAOSLO imaging locations denoted by the small numbered boxes. AMD1 has large soft drusen, AMD2 has geographic atrophy and AMD3 has reticular drusen. FAOSLO imaging locations were selected in areas beyond the clinically detectable lesions; these images are shown in Fig. 3.

The intensity of the image varied considerably between each location imaged and between patients. Continuous cell mosaics were seen in some locations in some AMD eyes (e.g. AMD2-1, shown in Fig. 3(c), whereas the cells were sparse in others (e.g. AMD1-2, shown in Fig. 3(b)). Despite the low contrast of the images, our automated algorithm was able to extract cell boundaries. However, the AMD patient images required more manual correction than

#197058 - $15.00 USD Received 3 Sep 2013; revised 9 Oct 2013; accepted 12 Oct 2013; published 18 Oct 2013

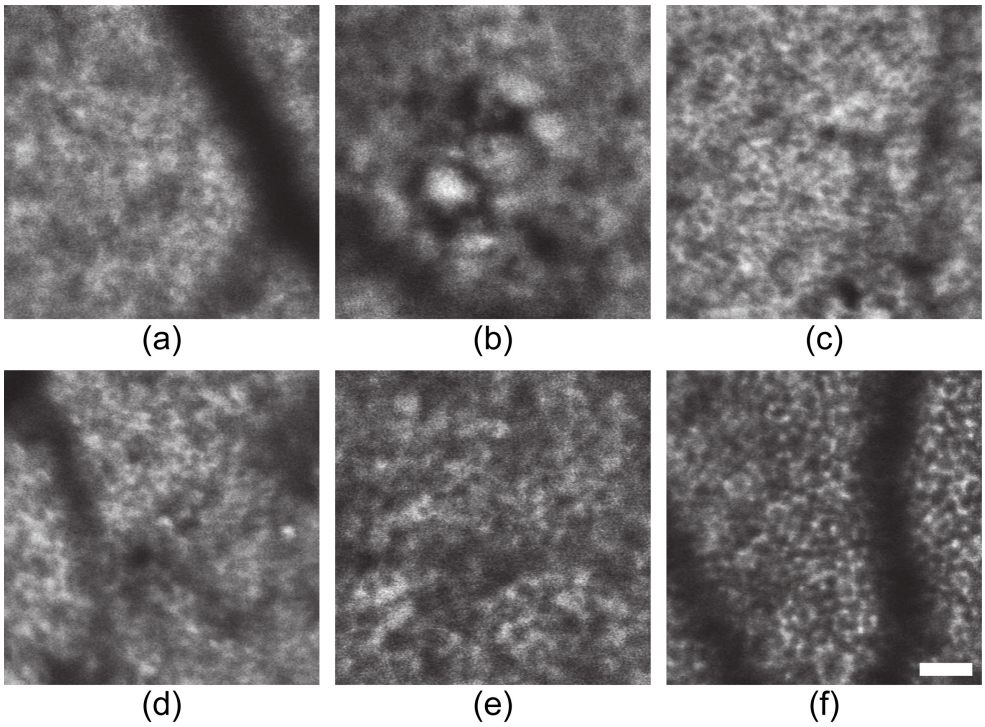

Fig. 3. Fluorescence adaptive optics images of the RPE mosaic at locations marked in Fig. 2 for (a) AMD1-1 (b) AMD1-2 (c) AMD2-1 (d) AMD2-2 (e) AMD3-1, and (f) normal young control-1. Scale bar is 50 µm.

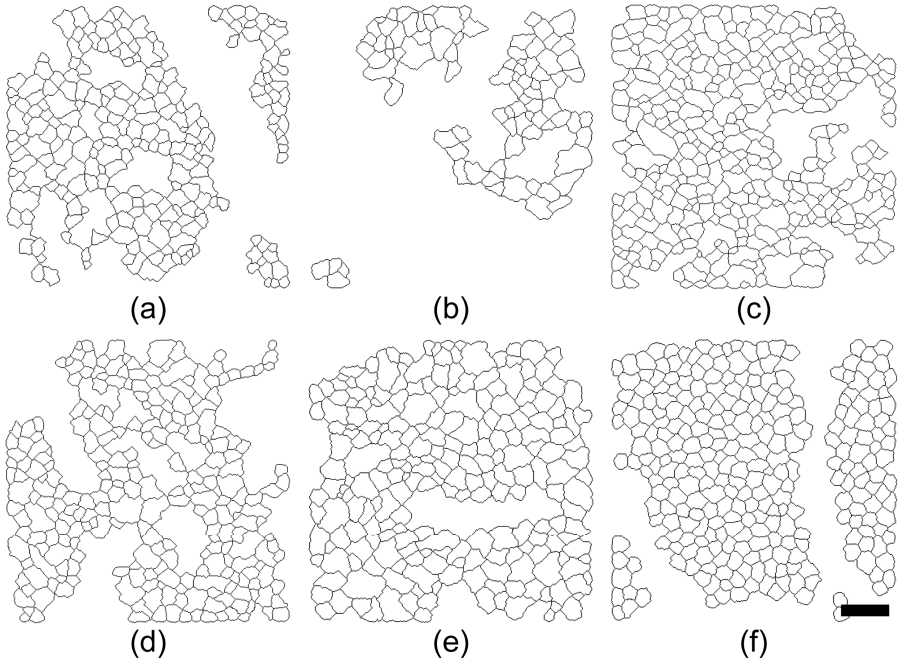

Fig. 4. Segmented RPE cells from FAOSLO images shown in Fig. 3. (a) AMD1-1 (b) AMD1-2 (c) AMD2-1 (d) AMD2-2 (e) AMD3-1, and (f) normal young control-1. Scale bar is 50 µm.

#197058 - $15.00 USD Received 3 Sep 2013; revised 9 Oct 2013; accepted 12 Oct 2013; published 18 Oct 2013

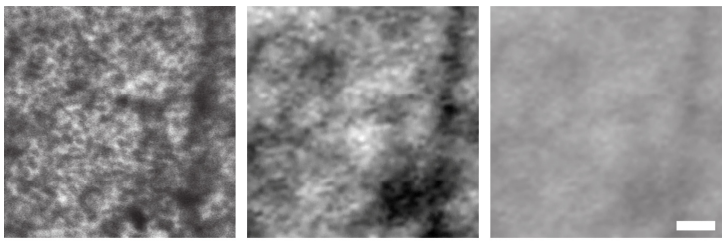

Fig. 5. Despite fairly uniform FAF in cSLO, RPE mosaic imaged in AOSLO shows deviation from normal morphology. (a) Location 2 from AMD2 in FAOSLO (from Fig. 4(c)), compared to corresponding area imaged in FAF cSLO Spectralis, where some structure can be seen, but individual cells are not resolved, contrast has been stretched in (b) for comparison to AOSLO and original FAF image without contrast adjustment. Scale bar is 50 µm.

those from normal eyes. Segmented cells after manual correction are shown in Fig. 4. Comparison of cSLO and FAOSLO images shows that the cSLO FAF image can be fairly uniform and 'normal' appearing despite abnormal RPE morphology (Fig. 5(c)). For comparison here in Fig. 5(b), the cSLO image contrast is scaled so that the minimum pixel value is zero and the maximum is 255.

Cell areas across small ~1 degree fields (300 x 300 µm) were quite uniform in the young normal eye, but exhibited high variance in the AMD eyes. This is illustrated in Fig. 6, which shows segmented RPE cells colored by area and shown graphically with the corresponding histograms below each image.

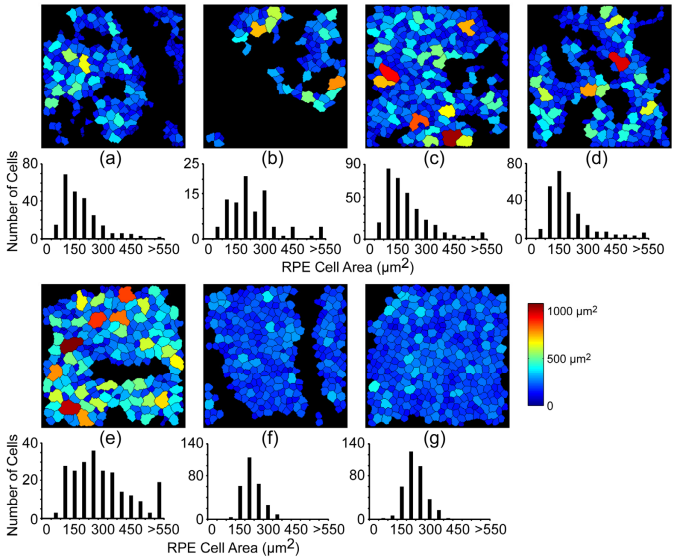

Fig. 6. AMD eyes show greater variance in cell area. Segmented cells colored by area for: (a) AMD1-1, (b) AMD1-2, (c) AMD2-1, (d) AMD2-2, (e) AMD3-1, (f) normal young control-1 and (g) normal young control-2. Color bar shows relation between color and area. Below each image is the corresponding histogram of cell sizes. Note the difference in number of cells for each image (y-axis of each histogram); bin sizes are identical. Normal eyes show a tight, fairly normal distribution of sizes (histograms below (f) and (g)), while the AMD eyes (histograms below a-e) show larger variance, with both larger and smaller cells.

4. Conclusions

RPE imaging in FAOSLO in patients with AMD remains challenging. Improvements that we anticipate will further increase performance are eye tracking based image stabilization and the

#197058 - $15.00 USD Received 3 Sep 2013; revised 9 Oct 2013; accepted 12 Oct 2013; published 18 Oct 2013

use of achromatizing lenses. Eye tracking and stabilization of the imaged area will allow for a more controlled light exposure and more uniform signal to noise ratio in the registered image average. Currently, as the eye moves around, the locations on the edge of the frame drift in and out of the imaging field. An appropriately designed achromatizing lens placed at the exit pupil of the system could potentially also improve performance. We used a broad band emission filter here to increase our fluorescence signal, but this causes the light distribution at the detector to elongate axially along the path of the beam as each wavelength focuses at different positions. An achromatizing lens can make this light distribution more compact, causing the light emitted at different wavelengths from individual lipofuscin granules to focus at the same position axially. This should improve both axial resolution and throughput.

This method might be further optimized by the use of higher light levels, such as those used by Morgan et al. in their 2009 paper [17], and permitted under the current ANSI standard [24]. This could potentially allow images to be obtained more rapidly and/or facilitate the use of a smaller confocal aperture that could improve resolution. However, we chose to use very conservative light levels here for two main reasons. The first is our concern for patient safety, particularly for the AMD retina, which may be more susceptible to damage from visible light exposures. The second is that the ANSI standards will soon be updated based upon new data, such as that obtained by Morgan et al. [26,27], and the forthcoming standards will be more conservative [39].

Many of the images we obtained in AMD eyes appeared to be in focus, but did not contain structure indicative of individual cells, particularly in areas that already have detectable lesions (not shown). This makes interpretation of these images difficult as it remains ambiguous as to whether the cellular features were not present due to our inability to image them or if they are truly absent. This is a familiar problem for those using *in vivo* imaging methods. Many of the RPE cell morphologies seen in the later stages of AMD, such as multi-layered cells and heaping and sloughing of cells could disrupt our ability to see cellular structure [5]. The AF imaging technique in FAOSLO capitalizes on the fact that the normal RPE is arranged in a flat monolayer. It is thought that the contrast arises due to the nucleus of the cell providing contrast to the bright lipofuscin laden surround (this has not been confirmed however). When the RPE is disrupted in disease it is not clear if we might expect to see any contrast between the center and surround of the cell using this imaging method. Additionally, data is needed to distinguish normal changes related to aging from disruptions related to disease in FAOSLO images of the RPE cell mosaic.

Although still imperfect, the focusing method proposed here has provided us with the first *in vivo* glimpse of the RPE mosaic in AMD. The images we obtained look very similar to those seen in histology from AMD donor eyes, such as the image shown in supplementary Fig. 5 of Kaneko and colleagues [4]. One surprising finding is that RPE morphology was disrupted in areas that have relatively normal appearing RPE fluorescence in conventional commercial cSLO FAF images (Fig. 5). This demonstrates that despite a uniform fluorescence signal in low resolution imaging, the underlying RPE morphology can be irregular. Further work is needed to characterize how these changes in the RPE mosaic relate to the changes to photoreceptors seen in reflectance FAOSLO images and the overall pattern of fluorescence seen in cSLO FAF images.

Acknowledgments

The authors wish to thank Jennifer J. Hunter, Ph.D. for helpful discussions concerning light safety. This work was supported by NIH grants F32EY021669, EY021786, EY014375, EY004367, and EY007125, a postdoctoral award to Ethan A. Rossi, Ph.D., from Fight for Sight (FFS-PD-11-020), a grant from the Edward N. & Della L. Thome Memorial Foundation to Mina M. Chung, M.D. Alfredo Dubra-Suarez, Ph.D., holds a Career Award at the Scientific Interface from the Burroughs Wellcome Fund and a Career Development Award from Research to Prevent Blindness. This research was also supported by unrestricted departmental grants from Research to Prevent Blindness.